First release of Apertif imaging survey data

A&A 667, A38 (2022)
https://doi.org/10.1051/0004-6361/202244007

Astronomy & Astrophysics

First release of Apertif imaging survey data

E. A. K. Adams[1,2], B. Adebahr[3], W. J. G. de Blok[1,4,2], H. Dénes[1], K. M. Hess[5,1,2], J. M. van der Hulst[2], A. Kutkin[1,6], D. M. Lucero[7], R. Morganti[1,2], V. A. Moss[8,9,1], T. A. Oosterloo[1,2], E. Orrú[1], R. Schulz[1], A. S. van Amesfoort[1], A. Berger[3], O. M. Boersma[10], M. Bouwhuis[11], R. van den Brink[1,21], W. A. van Cappellen[1], L. Connor[10,12], A. H. W. M. Coolen[1], S. Damstra[1], G. N. J. van Diepen[1], T. J. Dijkema[1], N. Ebbendorf[1], Y. G. Grange[1], R. de Goei[1], A. W. Gunst[1], H. A. Holties[1], B. Hut[1], M. V. Ivashina[13], G. I. G. Józsa[14,15], J. van Leeuwen[1,10], G. M. Loose[1], Y. Maan[16,1], M. Mancini[1], Á. Mika[1], H. Mulder[1], M. J. Norden[1], A. R. Offringa[1,2], L. C. Oostrum[1,10,17], I. Pastor-Marazuela[10,1], D. J. Pisano[18,19,4], A. A. Ponomareva[20], J. W. Romein[1], M. Ruiter[1], A. P. Schoenmakers[1], D. van der Schuur[1], J. J. Sluman[1], R. Smits[1], K. J. C. Stuurwold[1], J. Verstappen[2,1], N. P. E. Vilchez[1], D. Vohl[10,1], K. J. Wierenga[1], S. J. Wijnholds[1], E. E. M. Woestenburg[1], A. W. Zanting[1], and J. Ziemke[1,22]

(Affiliations can be found after the references)

Received 12 May 2022 / Accepted 5 August 2022

ABSTRACT

Context. Apertif is a phased-array feed system for the Westerbork Synthesis Radio Telescope, providing forty instantaneous beams over 300 MHz of bandwidth. A dedicated survey program utilizing this upgrade started on 1 July 2019, with the last observations taken on 28 February 2022. The imaging survey component provides radio continuum, polarization, and spectral line data.

Aims. Public release of data is critical for maximizing the legacy of a survey. Toward that end, we describe the release of data products from the first year of survey operations, through 30 June 2020. In particular, we focus on defining quality control metrics for the processed data products.

Methods. The Apertif imaging pipeline, `Apercal`, automatically produces non-primary beam corrected continuum images, polarization images and cubes, and uncleaned spectral line and dirty beam cubes for each beam of an Apertif imaging observation. For this release, processed data products are considered on a beam-by-beam basis within an observation. We validate the continuum images by using metrics that identify deviations from Gaussian noise in the residual images. If the continuum image passes validation, we release all processed data products for a given beam. We apply further validation to the polarization and line data products and provide flags indicating the quality of those data products.

Results. We release all raw observational data from the first year of survey observations, for a total of 221 observations of 160 independent target fields, covering approximately one thousand square degrees of sky. Images and cubes are released on a per beam basis, and 3374 beams (of 7640 considered) are released. The median noise in the continuum images is 41.4 uJy beam^{-1}, with a slightly lower median noise of 36.9 uJy beam^{-1} in the Stokes V polarization image. The median angular resolution is $11.6''/\sin\delta$. The median noise for all line cubes, with a spectral resolution of 36.6 kHz, is 1.6 mJy beam^{-1}, corresponding to a 3-σ H I column density sensitivity of 1.8×10^{20} atoms cm^{-2} over 20 km s^{-1} (for a median angular resolution of $24'' \times 15''$). Line cubes at lower frequency have slightly higher noise values, consistent with the global RFI environment and overall Apertif system performance. We also provide primary beam images for each individual Apertif compound beam. The data are made accessible using a Virtual Observatory interface and can be queried using a variety of standard tools.

Key words. surveys – radio continuum: galaxies – polarization – radio lines: galaxies – galaxies: ISM

1. Introduction

Large, untargeted surveys have always been a driver of new discoveries in astronomy, across all wavelength bands. Surveying wide areas of sky or large volumes of the Universe provides large samples of astronomical sources, including many rare and interesting objects.

In the radio regime, surveys have generally fallen into two categories in the past, based on technological limitations. In the first category, radio continuum and polarization surveys utilize interferometers for higher angular resolution with backends that provide a large bandwidth but limited spectral resolution. The prototypical example of a such survey that continues to provide a rich legacy dataset is the NRAO VLA Sky Survey (NVSS) (Condon et al. 1998). The subsequent VLA Faint Images of the Radio Sky at Twenty-Centimeters (FIRST) survey demonstrates the power of even higher angular resolution (White et al. 1997). More recently the VLA Synoptic Sky Survey at slightly higher frequencies is pushing to higher angular resolution and better sensitivity (Lacy et al. 2020), while the Rapid ASKAP Continuum Survey (McConnell et al. 2020; Hale et al. 2021), at slightly lower frequencies, is increasing the resolution and sensitivity of radio surveys available in the Southern Hemisphere. Complementary surveys at low frequencies provide an important view of the radio continuum sky. An early example is the Westerbork Northern Sky Survey (WENSS; Rengelink et al. 1997). Recently, the low-frequency window is expanding with a wealth of new low-frequency radio continuum and polarization surveys, including the LOFAR Two-metre Sky Survey (LoTSS; Shimwell et al. 2019), the LOFAR LBA Sky Survey (LoLSS

de Gasperin et al. 2021), and the GaLactic and Extragalactic All-Sky MWA Survey (GLEAM, Wayth et al. 2015).

In the second category, spectral line surveys, notably of neutral hydrogen (H I) at 21 cm, require high spectral resolution. The largest untargeted H I surveys to date rely on single-dish telescopes, lacking spatial resolution, both to provide sensitivity and backends with the required high spectral resolution over relatively large bandwidths, both of which are necessary to enable effective surveys. The state of the art for H I surveys is the Arecibo Legacy Fast ALFA H I survey (ALFALFA, Haynes et al. 2018), with the H I Parkes All-Sky Survey (HIPASS, Meyer et al. 2004) providing a complementary view in the Southern Hemisphere.

While historically radio continuum and polarization surveys have been distinct from spectral line surveys, the new generation of backends for interferometric radio telescopes can handle large bandwidths at high spectral resolution. The large bandwidth provides for sensitive radio continuum and polarization data while the high spectral resolution enables spectral line observations. Another key technological advance is the development of phased-array feeds (PAFs), which provide a large number of beams on the sky, and hence large fields of view. Thus, a new generation of interferometers operating at GHz frequencies provide the spatial resolution, sensitivity, and field-of-view necessary to efficiently carry out cutting-edge surveys both for H I and for radio continuum and polarization (Maddox et al. 2016). Examples of this include: the MeerKAT International GigaHertz Tiered Extragalactic Exploration (MIGHTEE) survey with MeerKAT, originally designed as continuum survey but which is simultaneously a sensitive H I survey (Jarvis et al. 2016; Maddox et al. 2021); and the synergy between the surveys on ASKAP, where the H I-focused Widefield ASKAP *L*-band Legacy All-sky Blind surveY (WALLABY; Koribalski et al. 2020) provides a higher frequency measurement to complement the lower frequency the radio continuum and polarization surveys, Evolutionary Map of the Universe (EMU, Norris et al. 2021) and Polarisation Sky Survey of the Universe's Magnetism (POSSUM, Gaensler et al. 2010). This synergy between different observing frequencies can also extend to looking at spectral lines in both absorption and emission, such as between WALLABY and the First Large Absorption Survey in H I (FLASH, Allison et al. 2022).

Another example is the PAF upgrade to the Westerbork Synthesis Radio Telescope (WSRT), the APERture Tile In Focus array (Apertif), fully described in van Cappellen et al. (2022). Apertif is a complex system; here, we briefly summarize the most relevant aspects from the perspective of an imaging science user. The Apertif system consists of PAFs with 121 Vivaldi elements on 12 of the 14 WSRT dishes, including dishes RTC and RTD which provide the longest baselines (and highest angular resolution). The signal from these elements can be combined to form forty simultaneous beams on the sky, each with a typical half-power size of 35′, significantly increasing the instantaneous field of view of WSRT to ∼8 deg^2 at 50% of the peak sensitivity. The layout of the beams is shown in figure 25 of van Cappellen et al. (2022). The Apertif system provides 300 MHz of contiguous bandwidth within the frequency range 1130–1750 MHz. At the dish level, the 300 MHz bandwidth is divided into 384 subbands of 781.25 kHz each. The backend can be configured to provide an imaging correlator which further divides each subband into 64 channels of 12.2 kHz.

Following this upgrade, WSRT-Apertif was dedicated to large survey programs: a time-domain survey (Maan & van Leeuwen 2017; van Leeuwen et al. 2022) and a two-tiered imaging survey (Hess et al., in prep.). The legacy of a survey is greatly enhanced by the release of high quality science-ready data products to the community. Toward that end, we present the first release of Apertif imaging survey data, covering the first year of survey operations, 1 July 2019–30 June 2020. In this first data release, the emphasis is on releasing the best quality data products from a first processing to the community as rapidly as possible to demonstrate the potential of the Apertif imaging surveys.

The paper is organized as follows: Sect. 2 introduces the Apertif imaging surveys, and the observations covered by this release. Section 3 describes the released data products, including the choice for which of these to release. The quality of the continuum, polarization, and spectral line data is discussed in Sects. 4, 5, and 6. In Sect. 7, we detail known caveats and limitations of the Apertif system and data, and we strongly encourage the reader to carefully read this section. We highlight the science potential of the Apertif imaging surveys in Sect. 8. In Sect. 9, we briefly describe future prospects and improvements for further data releases. Finally, Sect. 10 offers a brief summary of the data release. Appendix A provides information on available data from pre-survey operations, including a science verification campaign (SVC) undertaken to verify the scientific performance of the Apertif system and early science observations between the SVC and start of survey operations. A companion paper, Kutkin et al. (2022, hereafter K22), presents a continuum source catalog for the first data release.

2. The Apertif imaging surveys

The wide field-of-view of Apertif, the spectral resolution of 12.2 kHz across a large bandwidth of 300 MHz, and an angular resolution of up to 11″/sin δ enable large-scale, simultaneous surveys of the radio continuum, polarization, and spectral line sky. Toward this end, a significant fraction of the Apertif observing time has been dedicated to a legacy survey program consisting of two tiers of imaging surveys: a wide and medium-deep tier, referred to respectively as the Apertif Wide-area Extragalactic Survey (AWES) and the Apertif Medium-deep Extragalactic Survey (AMES). The wide tier aims to cover a relatively large region of the sky, while the medium-deep tier focuses on a smaller region of sky, visiting individual fields up to ten times in order to build up sensitivity, with the ultimate goal of achieving a column density sensitivity of $\sim 5 \times 10^{19}$ atoms cm^{-2} in order to detect low surface brightness H I. The repeated observations of the medium-deep tier also enable variability studies.

The design of the imaging surveys was driven by a broad set of extragalactic science goals, including:

– Investigate gas and total dynamical mass distribution (derived from gas kinematics) over a wide range of galaxy properties, using resolved H I observations;

– Investigate environment and the role of interactions, gas accretion and removal of gas;

– Investigate the properties of the smallest gas-rich galaxies in the local Universe;

– Study the role of cold gas in active galactic nuclei (AGN) and their feedback activity;

– Study the history of star formation and AGN activity of the faint radio continuum population;

– Study the magnetic fields in galaxies and of the large-scale structures in which they are embedded.

With these goals in mind, the footprint of the Apertif imaging surveys was selected to maximize multiwavelength coverage,

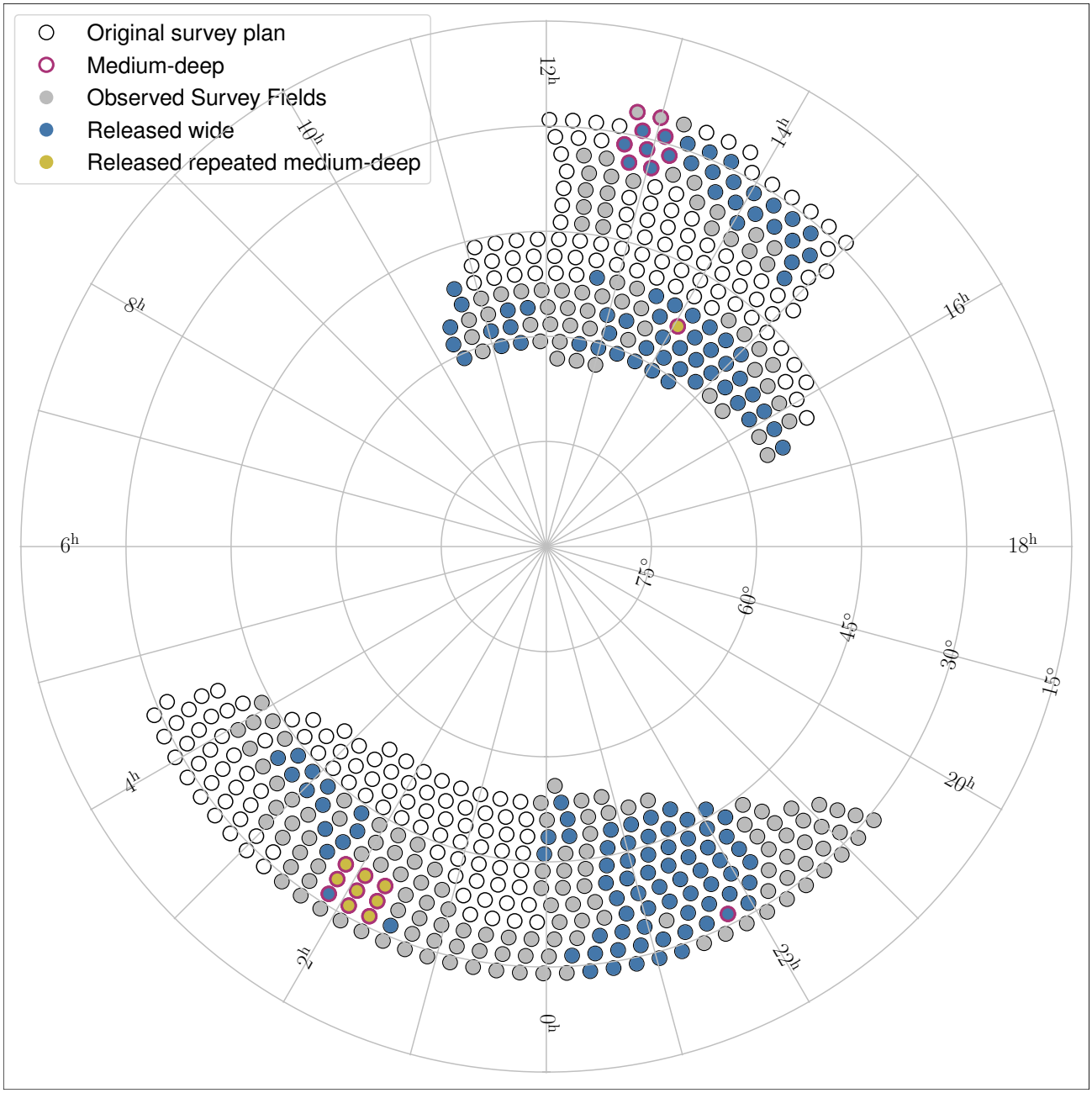

Fig. 1. Sky view of Apertif imaging observations. Blue circles indicate wide observations (single visit) while pink circles indicate fields with multiple visits as part of this data release (but we note that data products are only released for individual observations). The open black circles indicate the coverage in the original 4-yr survey plan. Grey circles show Apertif observations to date; these effectively represent the final survey footprint. Circles outlined in purple have medium-deep coverage in the full survey.

especially optical redshifts to provide distances for radio continuum sources. Other considerations included maximizing overlap with LoTSS (Shimwell et al. 2019), providing a large coverage in Right Ascension, and maximizing scheduling feasibility and efficiency. Figure 1 provides an overview of the imaging survey footprint. The full sky coverage of the original 4-yr survey plan is shown for reference; filled circles indicate the effective final coverage of the Apertif imaging surveys (colored circles are contained within this data release). Fields that have medium-deep coverage in the full survey are also highlighted in Fig. 1. There are two main regions of interest for the medium-deep tier: the Perseus-Pisces supercluster, a rich environment, and the *Herschel*-ATLAS North Galactic Pole field (Smith et al. 2017), which has large amounts of ancillary data available. In addition, there are two individual fields hosting intra-hour variables with medium-deep coverage. Hess et al. (in prep.) provide a detailed discussion on the science cases, chosen footprint, and tiling strategy.

During the first year of survey observations, medium-deep observations were focused on the Perseus-Pisces field. An additional medium-deep field containing the first intra-hour variable found in the Apertif imaging surveys (Oosterloo et al. 2020) was also included. The wide observations focused on coverage between 10 and 16 h RA with Dec > 45° to maximize overlap with publicly available LoTSS data. Wide observations in the same RA range but at lower Dec were also carried out to start

Table 1. Available data products.

Data product	Format	Dimensions [a]	Size per beam	Size per observation
Level zero data products				
Survey field raw visibility data	MS	4×24576	117 GB	4.7 TB
Calibrator raw visibility data	MS	4×24576	1.6–2.6 GB [b]	64–104 GB [b]
Level one data products				
Calibration tables	MS table	–	660 MB	26.3GB
Self-calibrated visibility data	uvfits	4×12288	58 GB	2.3 TB [c]
Level two data products				
Continuum				
Multi-frequency synthesis beam images	fits	3073×3073	37 MB	1.5 GB
Polarization				
Stokes Q and U cubes	fits	$2049 \times 2049 \times 24$	1.5 GB	62 GB
Stokes V multi-frequency synthesis image	fits	3073×3073	37 MB	1.5 GB
Line				
Continuum-subtracted, dirty line cubes	fits	$661 \times 661 \times 1218$	8 GB [d]	320 GB [d]
Restoring beam cubes	fits	$661 \times 1321 \times 1218$	320 GB [d,e]	640 GB [d,e]

Notes. [a]For level zero and one data: number of polarizations and channels. For level two data: image/cube sizes. [b]Data sizes are after pruning, to only keep the Apertif beam that contains that calibrator, and the range of values is for different calibrator scan lengths. [c]Maximum size; files can be smaller depending on flagging within pipeline. [d]Total size for four line beam^{-1} cubes produced. [e]After symmetric reduction.

building coverage around the second medium-deep footprint. The wide tier in the first year also included significant coverage at 22–0 h RA for maximizing schedule efficiency.

The two tiers share a common observing strategy and observational setup. Survey fields are observed for 11.5 h as a compromise between flexibility in scheduling and the depth/maximum *uv* coverage of a full 12 h synthesis imaging track[1]. Calibrator observations alternate between a flux/bandpass (3C147 or 3C196, occasionally 3C295) and polarization calibrator (3C286 or 3C138); calibrators are observed in every Apertif beam, necessitating forty separate calibrator observations. The calibrator scans vary from 3–5 min in length per compound beam, depending upon the available gap until the next survey field. Up to two survey fields can be observed in a row; thus a survey field may be separated in time from its calibrator by up to ∼15 h. Occasionally an observing session will start or end with a survey field in order to increase observing efficiency; then the separation in time may be longer. In order to validate the long-time separation between calibrators and target fields, we checked calibration gain solutions over the course of a full observing run (10 days). The amplitude solutions varied by less than 10% over the full period, demonstrating that a longer period between calibration scans should have minimal impact on the absolute calibration. Hess et al. (in prep.) describes the automation and details of the survey scheduling. As the main spectral line of interest is H I, the observations use the lowest frequency settings, covering the band 1130–1430 MHz, corresponding to a maximum redshift of 0.26 for H I. This band offers a large cosmic volume for observing H I; however, the lower half of the band is significantly affected by RFI and thus no derived data products are offered for it (see Sect. 3.3.2)[2]. The 24576 channels provide a frequency resolution of 12.2 kHz, or 2.6–3.2 km s^{-1} across the band for H I, but spectral line data products are typically produced with a spectral binning to 36.6 kHz. The angular resolution of the imaging survey observations is $11–15'' \times 11–15''/\sin(\delta)$, as the exact resolution depends on the weighting used. Continuum and polarization data are imaged with uniform weighting to provide the highest angular resolution, close to 11″, while the line cubes are produced with a resolution of ∼15″ and increased surface brightness sensitivity. We emphasize that the two outlying dishes, RTC and RTD, are required for full angular resolution. The achieved noise in a single observation is ∼40 μJy beam^{-1} in the continuum images and ∼1.6 mJy beam^{-1} over 36.6 kHz in the line cubes.

3. Data release

This section describes the released Apertif data products. All data from the first year of survey observations are considered for release. This includes all raw observational data, and a selection of processed data. In order to balance data quality against the timeliness of a prompt release, processed data products are only released if the continuum image passes validation as described in Sect. 4.1. This decision is further motivated below in Sect. 3.3.2. An overview, including the original size, of all Apertif data products is provided in Table 1.

3.1. Apercal processing

Survey observations are automatically processed by `Apercal`[3], the Apertif imaging and calibration pipeline, via an automated trigger, `autocal`. Full details of this pipeline are provided in Adebahr et al. (2022b). A brief description of the processing is provided below.

The `Apercal` pipeline is a modular pipeline written in python using common astronomical software. Apercal processes

[1] As WSRT is an east-west array, Earth rotation aperture synthesis is critical for *uv* coverage.

[2] We note that for survey observations starting from February 2021 the observing band changes to 1220–1520 MHz to provide the largest RFI-free band possible.

[3] Publicly available at https://github.com/apertif/apercal

Table 2. VO tables for Apertif DR1.

Table name	url [(a)]	Obscore type	Obscore subtype
Level two data products			
apertif_dr1.continuum_image	/apertif_dr1_continuum_images/form	image	continuum
apertif_dr1.pol_cubes	/apertif_dr1_polarization_cubes/form	cube	polarization cube
apertif_dr1.spectral_cubes	/apertif_dr1_spectral_cubes/form	cube	spectral cube
apertif_dr1.beam_cubes	...	cube	dirty beam
Level one data products			
apertif_dr1.calibrated_visibilities	/apertif_dr1_calibrated_visibilities/form	visibility	calibrated visibility
Level zero data products			
apertif_dr1.raw_visibilities	/apertif_dr1_raw_visibilities/form	visibility	raw visibility
apertif_dr1.flux_cal_visibilities	/apertif_dr1_flux_cal_visibilities/form	visibility	raw visibility
apertif_dr1.pol_cal_visibilities	/apertif_dr1_pol_cal_visibilities/form	visibility	raw visibility

Notes. [(a)]The URL are expressed relative to https://vo.astron.nl/apertif_dr1/q

each beam of an Apertif observation individually, following standard reduction procedures. First, the data is split to only keep frequency ranges mostly free of radio frequency interference (RFI). Experience showed that removing frequency ranges dominated by RFI significantly improved the calibration and quality of the data at all frequencies. For the data under consideration for the data release, this meant splitting to keep the upper 150 MHz of the band, 1280–1430 MHz, and additionally flagging the first 12.5 MHz, in order to avoid persistent RFI, resulting in an effective frequency range of 1292.5–1430 MHz. The data is then flagged, both for a-priori known flags[4] and for RFI using `AOFlagger`, including special adaptations for Apertif (Offringa et al. 2012). A standard cross-calibration (including of cross-hand data products) is then done using `CASA` tasks (McMullin et al. 2007). A direction-independent self-calibration is undertaken in `miriad` (Sault et al. 1995) on data frequency-averaged to the subband resolution. As a first step, a phase-only parametric self-calibration based on FIRST and NVSS is undertaken; then the self-calibration iterations on the data are undertaken. Phase solutions are always found and applied to the data; amplitude solutions are always derived but only applied to the data if the subsequent dirty image with amplitude solutions improves on the dirty image with only phase solutions. Importantly, Apercal does not account for any direction dependent errors. Finally, the self-calibration solutions are applied and the imaging of the continuum, polarization and line data is done in `miriad`. For the continuum images, sources above 5-σ are identified and cleaned to a threshold of 1-σ, where σ is the "theoretical" noise, calculated as the noise in a Stokes V image. The same masks are applied to the polarization data and sources there are also cleaned to a 1-σ threshold. The model of the continuum emission is subtracted from the full spectral resolution data and line cubes are created[5]. We note that the line cubes are only imaged, meaning that emission is neither identified nor cleaned in them; for this reason the dirty beam cubes are also kept as a data product to enable later cleaning. Finally, the processed data products are automatically ingested back into the Apertif Long-Term Archive (ALTA).

3.2. Virtual Observatory interface

The released data products are exposed through standard Virtual Observatory (VO) protocols to facilitate their access and exploration to both general and specialized users. In particular, the protocols offered are the Tabular Access Protocol (TAP)[6] and the Simple Image Access protocol (SIA)[7].

The VO registry can be accessed also through a web browser[8], which presents all collections on the ASTRON VO registry, including APERTIF_DR1. Selecting one collection allows the user to interactively query through a form all data products of that given collection, which is sorted by data product type for Apertif DR1.

The above query capabilities are also possible through standard VO tools, such as using TOPCAT (Taylor 2005) via TAP. The table names to query the different DR1 collections are summarized in Table 2. Moreover, it is possible to query all the available dataproducts from Apertif DR1 at once by using the table *ivoa.obscore* and limiting the results to the apertif_dr1 by appending to the ADQL statement "`where obs_collection="apertif_dr1"`".

3.3. Extent of data release

All raw observational data from the first year of survey operations are released. A subset of processed data products, meeting specified quality assessment criteria, are also released. These two subsets of released data are discussed further below.

3.3.1. Raw observational data

From the first year of survey observations, there are 221 observations of 160 unique survey fields; with an effective field-of-view of 6.44 square degrees[9], these observations cover over 1000 square degrees of sky. There are eight medium-deep fields with

[4] It should be noted that while `Apercal` supports robust, unique flagging commands for any observation, the automated processing pipeline workflow (`autocal`) uses a standard set of flags for all observations. Thus it does not provide any additional flags due to known but temporary issues, such as stuck dishes that were not on source. When these issues occasionally arise, a manual processing is undertaken where appropriate flag commands are provided.

[5] As discussed in Sect. 6.2, over 75% of released cubes show no (or extremely minor) artifacts; of the remainder, 15% show significant artifacts. These artifacts include incomplete continuum subtraction, in addition to other data quality issues. Thus the single step of visibility-based continuum subtraction is sufficient in the majority of cases.

[6] http://www.ivoa.net/documents/TAP/

[7] http://www.ivoa.net/documents/SIA/

[8] At the address https://vo.astron.nl

[9] Based on a spacing between fields of 2.3° in Dec and 2.8° in RA.

multiple observations within this data release (64 observations in total, not evenly distributed among the fields); these fields are highlighted in Fig. 1.

The raw observational data is recorded in measurement-set (MS) format. The sizes of the original raw data are given in Table 1. A set of calibration scans consists of 40 separate observations taken in succession. For each calibrator scan only one beam contains the calibrator; all other beams not containing the calibrator are discarded to save on data volume. We note that the calibrator observations are taken at a higher time resolution than the survey fields (10 vs. 30 s) to allow better RFI excision due to their shorter integration time.

As can be seen in Table 2, the raw visibility data are provided as separate collections for the survey fields, flux calibrator and polarization calibrator observations. The tables can be joined to identify the associated calibrators for a target observation.

The raw observational data are not stored on disk but rather on tape at a national facility, SURFsara[10]. In addition, the raw data are currently being compressed to further save on data volume (Offringa 2016). Thus, the VO tools enable queries of these data products, but not direct access or download. The data release documentation[11] contains up-to-date information on how to access the data.

3.3.2. Processed data

Processed data products that can be used directly, or with minimum additional processing, are of the most interest to the broader scientific community. The choice to release processed data products is done on a beam-by-beam basis, based on the quality of the continuum image. The continuum data is used for the self-calibration, so an artifact-free continuum image is a good indication that the inherent data quality of the observation and the calibration are of a sufficient standard. This is also a practical choice as the structure of the ingested processed data in ALTA means that either all or no processed data for a given beam should be released. Thus, in order for processed data products for a given beam to be released, the continuum image must pass validation. This approach offers a compromise between releasing as much data as possible on a short timescale to the community while only releasing data that is of high enough quality to be of sufficient interest to the community.

Toward this end, we define quality metrics for continuum images, polarization images and cubes, and spectral line cubes in Sects. 4.1, 5.1 and 6.1. The metrics are focused on ensuring a minimum sensitivity and resolution, in addition to identifying significant artifacts in images. The continuum validation criteria in Sect. 4.1 must be satisfied for processed data products to be released. The criteria for polarization and spectral line data products do not need to be satisfied, but the data are released with clear flags that indicate if they fail; the frequency of this is discussed in Sects. 5.2 and 6.2. We additionally provide the metrics for all data products in the relevant VO tables.

A total of 7640 beams were considered for release; 3374 of these beams are included in this first data release. We note that the unreleased beams will be contained in future data releases with improved processing (see Sect. 9). The sky coverage of the released continuum images is available as a HiPS image[12].

There are two additional important notes that are relevant for these data products. First, processed data products are only available for the upper 150 MHz of the band; thus the processed data products are produced over the range 1280–1430 MHz. Moreover, the first 12.5 MHz of data are flagged due to persistent RFI, therefore the resulting central frequency is 1361.25 MHz. The nominal bandwidth is then 137.5 MHz, but effectively it could be smaller due to additional RFI flagging. Secondly, these data products are not primary-beam corrected; primary-beam images are provided separately (see Sect. 3.4); these may be used for mosaicking or for correction of individual images.

The available processed data products are briefly discussed below. The quality of the continuum images, polarization images and cubes, and spectral line cubes are discussed in more detail in Sects. 4, 5, and 6.

Calibrated visibility data. Calibrated visibility data, with cross-calibration and self-calibration solutions applied, are currently stored as an intermediate data product at full time and spectral resolution; this may change with future updates to save storage space. These are stored on tape with the raw data, and the data release documentation[13] should be consulted for access.

Continuum images. A multi-frequency synthesis (mfs) Stokes I image is created over the full frequency range (1292.5–1430 MHz) and saved as a fits file for each beam. The size of the continuum images is $3.4^\circ \times 3.4^\circ$ (3073×3073 pixels, with $4''$ pixel^{-1}). This extends well outside the primary beam response to account for cases where a strong source is in a sidelobe and needs to be included in the self-calibration model and cleaning. Sources at the 5-σ level should be identified and cleaned to the 1-σ level[14].

Polarization images and cubes. A mfs Stokes V image over the full bandwidth (1292.5–1430 MHz) is produced. This image matches the continuum image in spatial extent: $3.4^\circ \times 3.4^\circ$ (3073×3073 pixels, with $4''$ pixel^{-1}). In order to prevent bandwidth depolarization and enable rotation measure synthesis studies, Stokes Q and U cubes with a frequency resolution of 6.25 MHz are produced. The cubes have a smaller spatial extent of $2.7^\circ \times 2.7^\circ$ (2049×2049 pixels, with $4''$ pixel^{-1}) but still extend well beyond the primary beam.

Line and dirty beam cubes. Four line cubes over a set of different frequency ranges are produced. Table 3 summarizes the covered frequency ranges and provides the corresponding redshift range for H I. The lowest redshift cube is produced at full spectral resolution while other cubes are produced with a 3-channel averaging. These cubes have a spatial extent of $1.1^\circ \times 1.1^\circ$ (661×661 pixels, with $6''$ pixel^{-1}). As the Apercal pipeline does not provide source finding or cleaning of the line cubes, corresponding dirty beam cubes are also provided to allow offline cleaning of source emission. Originally these dirty beam cubes are produced with twice the spatial coverage of the line cubes to enable full cleaning[15]. These dirty beams cubes

[10] https://userinfo.surfsara.nl/
[11] http://hdl.handle.net/21.12136/B014022C-978B-40F6-96C6-1A3B1F4A3DB0
[12] Via https://hips.astron.nl/ASTRON/P/apertif_dr1/
[13] http://hdl.handle.net/21.12136/B014022C-978B-40F6-96C6-1A3B1F4A3DB0
[14] Because the Apercal masking procedure uses thresholds that also depend on the maximum value of the residual image (Adebahr et al. 2022b), if there are persistent artifacts in a residual image, the maximum number of clean cycles may be reached before sources down to the 5-σ level are included in the source mask.
[15] We take advantage of the symmetric nature of the WSRT restoring beam to trim the beam cubes in half around the North–South axis to halve the size of the beam cubes. A script and instructions for restoring the full beams cubes are available at https://github.com/apertif/trim_apertif_beam_cube

Table 3. H I data cube parameters.

Cube	Frequency range (MHz)	Frequency resolution (km s^{-1})	Redshift range	Velocity range [a] (kHz)	Velocity resolution [a,b] (km s^{-1})
Cube0	1292.5–1337.1	36.6	0.062–0.099	18678–29667	9.0
Cube1	1333.1–1377.7	36.6	0.031–0.065	9293–19634	8.5
Cube2	1373.8–1418.4	36.6	0.001–0.034	424–10170	8.0
Cube3	1414.5–1429.3	12.2	–0.006–0.004	–1865–1252	2.6

Notes. [a]Optical velocity definition, with $v = cz$. [b]For center of cube.

are provided as linked data products in the spectral cube VO table.

3.4. Related data products: Primary beam images

Important additional data products are the primary beam images for each of the forty Apertif beams. Currently, Apercal does not provide primary beam corrections to any data products. Instead, primary beam corrections are applied separately, which requires primary beam images. Due to the nature of the phased array feed, each Apertif compound beam has a unique primary beam response and thus primary beam images are required for each of the forty beams. As Apertif does not offer a holography mode, we undertake two different approaches for measuring the primary beam response: drift scans across extremely bright sources (Dénes et al. 2022) and reconstruction of the primary beam responses via comparison to the NVSS catalog with a Gaussian process regression technique (K22). For this first data release, the primary beams from the Gaussian process regression approach are released. K22 describes their derivation in detail, and the data release documentation contains information on how to best apply these primary beam images to the Apertif data, including how to scale the primary beam images with frequency.

4. Continuum image quality

This section describes the validation of the continuum images and provides an overview of the data quality. In addition, we report on the accuracy of the flux scale and astrometric precision.

4.1. Validation of continuum images

The continuum images of every beam are individually validated. The starting point of the validation is the residual images obtained after cleaning the continuum images, and the validation aims at checking to what extent these images contain only Gaussian noise. The premise is that any significant deviation from Gaussian noise in the residual image indicates issues with the calibration and reduction of the data.

The following parameters were derived for each residual image:

- $\sigma_{\rm in}$: noise in the inner half degree of the image[16];
- $\sigma_{\rm out}$: noise at the edge of the residual image, more than a degree from the centre;
- $b_{\rm min}$: the size of the minor axis of the restoring beam;
- $R = \sigma_{\rm in}/\sigma_{\rm out}$;
- Ex−2: area, in units of beam area, with values $<-2\sigma$ in the inner 0.5° of the residual image, in excess of what is expected from a purely Gaussian distribution;
- Neg10: the absolute value of the level (in units of $\sigma_{\rm out}$) where pixels with values below this level cover 10 beam areas within the inner 0.5° of the residual image.

Both $\sigma_{\rm in}$ and $\sigma_{\rm out}$ are determined in a robust way using the median of the absolute values. $\sigma_{\rm in}$ is the relevant noise for scientific analysis, including the contributions of imaging artifacts, while $\sigma_{\rm out}$ is a reasonable measure of the expected noise. $b_{\rm min}$ corresponds to the angular resolution in an image; it is chosen over the corresponding size of the major axis of the restoring beam ($b_{\rm max}$) as $b_{\rm min}$ depends only on the baselines available for an observation, while $b_{\rm max}$ depends also on the declination of an observation. R is a measure of the strength of artifacts left in the center of the residual image. Ex−2 is a measure of how much a residual image deviates from perfect Gaussian noise; in the case of perfect noise Ex−2 = 0. This metric is derived by comparing to a Gaussian corresponding to $\sigma_{\rm out}$. Figures 2 and 3 demonstrate the actual noise histograms and comparison Gaussian distributions. Neg10 is another measure of how much a residual image deviates from Gaussianity. We emphasize that it is defined as an absolute level, so the expected value for a pure Gaussian distribution is 3.2, and more positive values indicate significant (negative) calibration residuals. We note that we did not use the equivalent of the parameter Ex-2 or Neg10 based on positive deviations from Gaussianity (Ex+2, Pos10). This is because insufficient cleaning results in source emission remaining in the residual image which would then dominate the validation (see the upper right panel of Figs. 2 and 3).

We then set the following criteria to pass validation; in order for a continuum image to pass validation and be released its residual image must satisfy all four of the following requirements:

1. $\sigma_{\rm in} < 60$ μJy beam^{-1} [17].
2. $b_{\rm min} < 15''$.
3. $R < 1.225$.
4. $R < 1.15$ or Neg10 < 4.5 or Ex−2 < 400.

The first two criteria were chosen to ensure that minimum survey specifications were met. Criterion 1 ensures that the noise of the images is low enough to be considered survey quality and valid. Criterion 2 ensures a minimum angular resolution that is required to achieve the science goals and meet survey specification. The restoring beam can be larger when both dishes with the longest baselines (RTC and RTD) are missing from an observation, and observations that are missing both RTC and RTD are considered failed[18].

The second two criteria were set to ensure a minimum of imaging artifacts in continuum images. These criteria were determined by undertaking visual examination of a large set of

[16] Specifically, within the central 500 × 500 pixels.

[17] Since $\sigma_{\rm in}$ is always greater than $\sigma_{\rm out}$ this is also a criterion on $\sigma_{\rm out}$.

[18] Such observations are repeated for individual wide fields while for medium-deep fields the eventual combination with data that contain RTC and RTD provides the final required angular resolution.

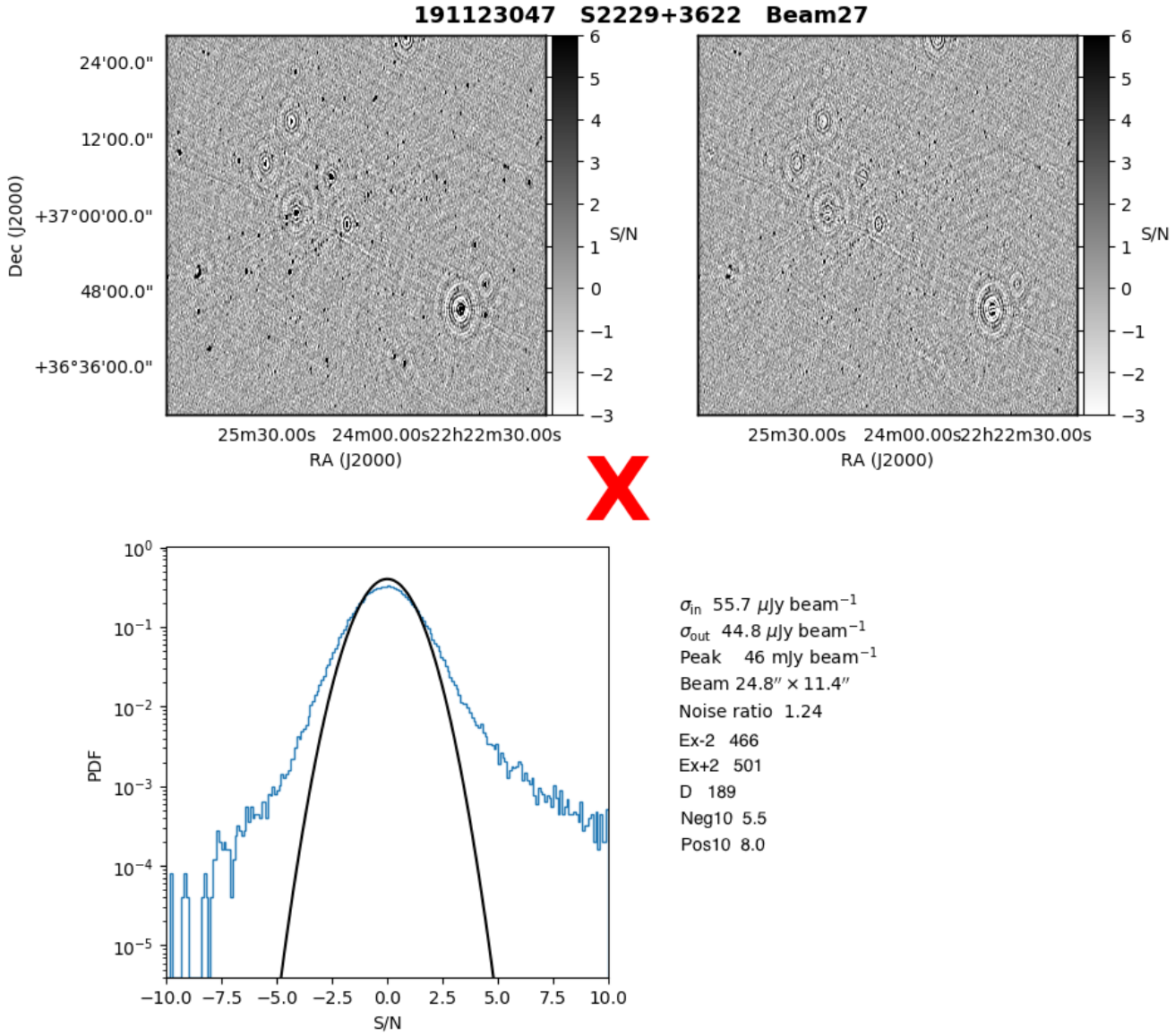

Fig. 2. Example of a continuum image that fails validation (as indicated by the red x); beam 27 of ObsID 191123047. The four panels shown are: *upper left:* continuum image; *upper right:* residual image (note the uncleaned source emission); *lower left:* flux density histogram of all pixels in the residual image (blue) compared to a Gaussian distribution (black) corresponding to $\sigma_{\rm out}$; *lower right:* statistics calculated for the beam. These include the metrics in Sect. 4.1, in addition to other statistics not (currently) used in the validation. The first five are: $\sigma_{\rm in}$, $\sigma_{\rm out}$, the peak in the continuum image, the restoring beam, and R. The next two are Ex−2 and Ex+2. The dynamic range (D) is calculated as the peak of the continuum image divided by Neg10 $\times\, \sigma_{\rm out}$. The final two statistics are Neg10 and Pos10.

images to determine numerical criteria that would catch significant image artifacts. The main types of image artifacts are due to errors in the self-calibration as well as strong direction-dependent errors for which the current calibration pipeline does not attempt to correct. Criterion 3 ensures that images do not have too much extra noise in the inner parts of the residual image, corresponding to left-over artifacts. Criterion 4 focuses on edges cases, where R is at intermediate values and additional constraints on large-scale structures and deviation from Gaussianity in the residual image are needed. We note that the first criterion can also eliminate images with significant artifacts if these increase the noise in the inner part of the image above the threshold. The criteria were set so that the large majority of images which were visually assessed as good would pass while minimizing the number of images visually assessed as bad which would pass.

Figures 2 and 3 provide an example of the diagnostic plots and validation metrics for two beams, one of which fails validation and one which passes. The image that fails validation has $\sigma_{\rm in}$ = 55.7 μJy beam^{-1}, $b_{\rm min}$ = 11.4″, R = 1.24, Ex−2 = 466, and Neg10 = 5.5; thus is fails both criteria 3 and 4. The validation metrics are provided for all released continuum images in the VO table.

4.2. Overview of released continuum image quality

Figure 4 provides an overview of the inner and outer noise values for all released (passed validation) continuum images. The median inner noise across all images, relevant for scientific analysis, is 41.4 uJy beam^{-1}. The median outer noise, indicative of what can be achieved with improved processing, is 36.1 uJy beam^{-1}. These values, along with uncertainties based on the 16th and 84th percentile ranges, are presented in Table 4.

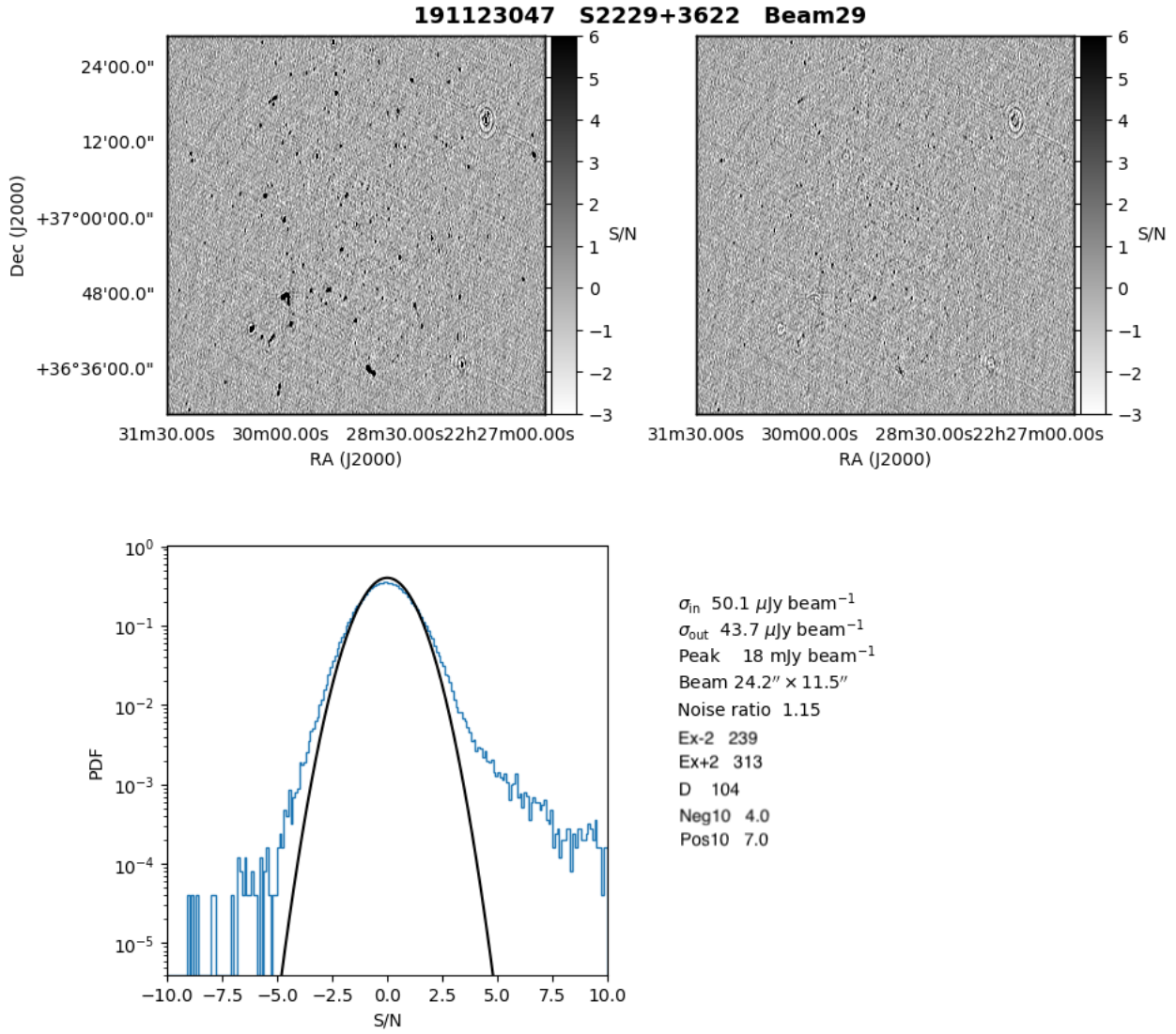

Fig. 3. Example of a continuum image that passes validation; beam 29 of ObsID 191123047. The panels are as in Fig. 2.

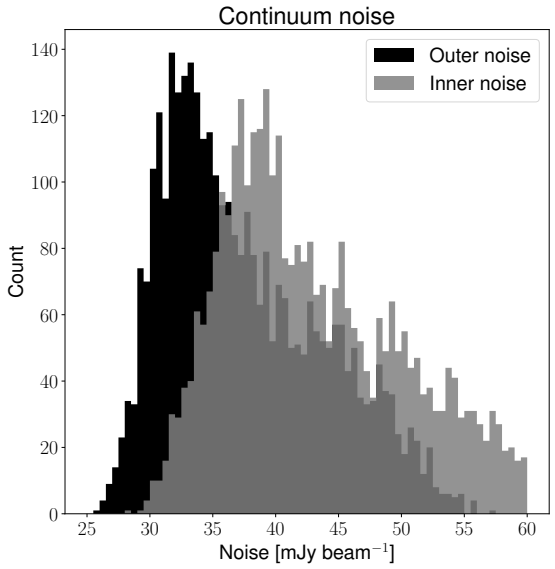

Fig. 4. Distribution of inner and outer noise for released continuum images.

Table 4. Typical noise values of released data products.

Data product	Released [a]	Passed [b]
Continuum image, inner region (μJy beam^{-1})	$41.4^{+9.5}_{-5.4}$	–
Continuum image, outer region (μJy beam^{-1})	$36.1^{+8.7}_{-4.9}$	–
Stokes *V* image, inner region (μJy beam^{-1})	$36.9^{+9.2}_{-4.8}$	$36.5^{+8.9}_{-4.4}$
Stokes *V* image, outer region (μJy beam^{-1})	$35.8^{+8.9}_{-4.5}$	$35.6^{+8.7}_{-4.3}$
Cube0 (mJy beam^{-1})	$1.66^{+0.33}_{-0.19}$	$1.64^{+0.31}_{-0.18}$
Cube1 (mJy beam^{-1})	$1.62^{+0.36}_{-0.19}$	$1.59^{+0.31}_{-0.17}$
Cube2 (mJy beam^{-1})	$1.60^{+0.35}_{-0.19}$	$1.56^{+0.32}_{-0.16}$

Notes. [a]For all released beams, which is based on the continuum image passing validation. [b]For only those beams which pass validation for the specified data product (good quality for line cubes, see Sect. 6.1); for continuum images this is the same as the released beams, while it is a subset for polarization and line.

The behavior of different compound beams is not identical. Specifically, the outer compound beams illuminate the edge of the field of view and thus may be expected to have a reduced

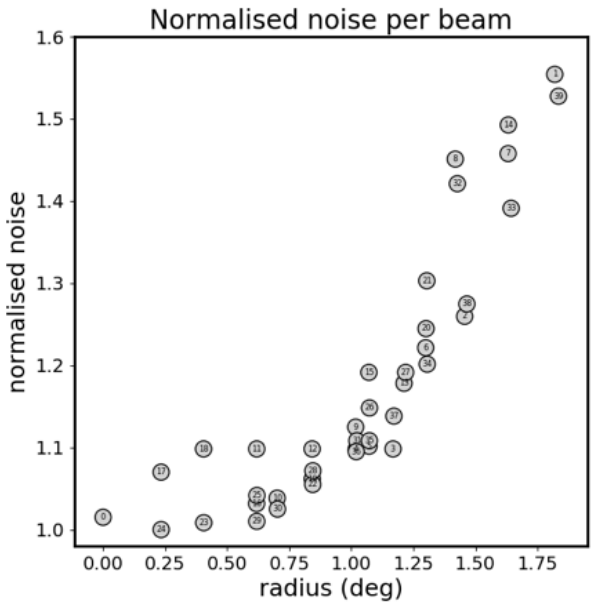

Fig. 5. Noise of continuum images for different Apertif beams, relative to the beam with the lowest noise (beam 24), as a function of distance from the pointing center. After mosaicking the noise is flatter.

sensitivity. This is demonstrated in figure 38 of van Cappellen et al. (2022) which shows the noise of continuum images in the compound beam layout, normalized to the beam with the lowest average noise, which is beam 24. Beams closer to the edge of the field of view have higher continuum noise values. Figure 5 quantifies this by showing the normalized noise as a function of distance from the pointing center of the PAF; the increased noise values track with distance. We note that mosaicking beams flattens the noise and reduces this effect.

4.3. Accuracy of flux scale

K22 assess the accuracy of the flux scale. They cross match the Apertif continuum catalog to the NVSS catalog and find that the flux scales match, which is by design of the primary beam derivation. They find a significant scatter in the flux ratios, which is a combination of multiple effects, including long-term variability of sources and the different angular resolution and sensitivities of the two catalogs. In order to assess the precision of the Apertif flux measurements, K22 compare flux measurements for medium-deep epochs with at least five observations, and find that flux variations across time indicate that the measurement precision is better than 10%, consistent with expected errors from cross-calibration.

4.4. Astrometric accuracy

K22 perform a cross-match of the Apertif radio continuum catalog to the public LoTSS catalog (Shimwell et al. 2022). As part of this cross-match they confirm the astrometry of the Apertif radio continuum images, finding that the typical offset between the Apertif and LoTSS sources is 0″ with a standard deviation of 2″ in both the RA and Dec directions.

We note that the self-calibration of the Apertif data begins with a parametric self-calibration using FIRST or NVSS data; thus the Apertif data is calibrated to the FIRST and NVSS astrometry by design.

5. Polarization data quality

Compared to the continuum images, there are a few important points to keep in mind for the polarization data quality. First, due to the physical nature of Stokes Q, U and V, astrophysical emission in the polarization images and cubes can be a positive or negative quantity while it can only be positive in Stokes I. Secondly, for Stokes Q and U cubes even faint artifacts in individual images can stack up, if present over the whole cube at a similar position, when the rotation measure synthesis technique is applied. This is also possible vice versa where strong artifacts in an individual image plane can be averaged out by rotation measure synthesis. Finally, Stokes V represents the circular polarization. Astronomically circularly polarized sources are extremely rare and most often show polarization fractions below 1%, so that Stokes V images should nominally be regarded as empty of astrophysical signal.

5.1. Validation of polarization images and cubes

After the overall calibration of the data, the quality of the polarization images and cubes is mostly influenced by the instrumental leakage characteristics of the primary beam. This means that the strongest artifacts often appear for sources far away from the beam centres where the instrumental leakage is higher. With this in mind we defined the following metrics, in addition to those in Sect. 4.1:

- $p_{\rm in}$: the maximum value of the absolute pixel values in the inner 0.5° of the image.
- $FT_{\rm max}$: the maximum of the absolute of a Fourier Transform of the image.

The validation of the polarization images and cubes provides information on their data quality; however, the release of polarization data products is based on the validation of the corresponding continuum image (Sect. 4.1), as detailed in Sect. 3.3.2. The Stokes V image and Stokes Q and U cubes have separate validation criteria, due to their different nature.

5.1.1. Validation of Stokes V images

In order for a Stokes V image to pass validation (as indicated by the data quality flag in the VO table), the following four criteria must all be satisfied:

1. $\sigma_{\rm in}$ and $\sigma_{\rm out} < 60$ μJy beam^{-1};
2. $b_{\rm min} < 15''$;
3. $FT_{\rm max} < 25$;
4. $p_{\rm in} < 4$ mJy.

The first two criteria were chosen to ensure minimum survey specifications were met and mirror the first two criteria for continuum images. Thus, generally a released Stokes V image will naturally pass those criteria as the (residual) continuum image has also passed them. Criterion 1 ensures a minimum sensitivity in the polarization images, and criterion 2 ensures the angular resolution.

The second two criteria were set to ensure a minimum of imaging artifacts in the Stokes V images. These criteria were determined by undertaking visual examination of a large set of Stokes V images. In addition to artifacts from errors in self-calibration and direction-dependent errors (which are caught by the continuum image validation, required for data release), leakage of strong sources near the primary beam edges also play a large role. In particular, criterion 4 eliminates images with strong instrumental leakage. Criterion 3 is designed to eliminate images with stripes due to unflagged RFI or bad amplitude

self-calibration solutions. The criteria were set so that the large majority of images which were visually assessed as good would pass validation while only a small fraction of images that were visually assessed as bad would pass.

5.1.2. Validation of the Stokes *Q* and *U* cubes

In order for Stokes Q and U cubes to pass validation (as indicated by the data quality flag in the VO table), at least two-thirds of the image planes within the cubes must satisfy both of the following criteria:

1. $b_{\rm min} < 17.5''$;
2. $\sigma_{\rm in}$ and $\sigma_{\rm out} < 300\,\mu{\rm Jy\,beam^{-1}}$.

The resolution requirement in criterion 1 is relaxed slightly compared to the continuum or Stokes V images due to the fact that the restoring beam becomes larger at lower frequencies. The noise requirement in criterion 2 is consistent with the requirement on the Stokes V images above, assuming 24 individual images covering the same total bandwidth, giving a factor of ∼5 increase in noise.

5.2. Overview of released polarization data quality

The validation of the polarization images and cubes is not required for release but is undertaken to provide information on their data quality. Generally, the validation of the polarization images and cubes follows that of the continuum very closely. This is due to the use of similar metrics and the fact that the continuum validation already excludes the majority of polarization images and cubes that would have large artifacts. Of the released 3374 beams, which are required to pass continuum validation (see Sects. 3.3.2 and 4.1), only 155 fail the Stokes V validation and 58 fail the Stokes Q and U validation and are flagged as such in the VO table. Generally, the reason a polarized data product might fail validation while the continuum image does not is due to a strong source at the edges of the image, where the leakage is largest. The validation status and metrics of the polarized data products are provided in the relevant VO table (see Table 2). In addition, there are 21 released beams that have no polarized data products because a polarized calibrator was unavailable for the observation 200309042 (S1042+5324).

The median inner and outer noise values across all Stokes V images are presented in Table 4, where the uncertainties indicate the 16th and 84th percentiles. There is essentially no difference in median noise values when considering all released Stokes V images, or only those that pass validation, supporting the release strategy outlined in Sect. 3.3.2 based on continuum image validation only.

In addition to the metrics presented here, Adebahr et al. (2022a) use polarization data from the SVC to place a limit of 1% on the polarization leakage down to the 30% response level of the primary beams.

6. Line cube quality

The quality of line cubes is dominated by different effects than the continuum or polarization data. While imperfect calibration or direction-dependent effects can impact the spectral line cubes, generally artifacts in the line cubes are dominated by two categories: imperfect continuum subtraction or bad frequency ranges (e.g., imperfect sub-bands at the system level).

It is useful to recall that four different line cubes are produced by Apercal; see Table 3 for a summary of their properties. The highest frequency cube (lowest redshift), cube3, is produced at the highest spectral resolution. Thus, it will have different noise properties compared to the other cubes. The RFI environment generally worsens at lower frequencies, so cube0 will be more strongly affected by RFI than cube1, for example.

6.1. Validation of line cube quality

The validation of the line cubes focused on the three lower spectral resolution cubes, as a common set of metrics could be defined for them. In practice, the quality of the high spectral resolution, high frequency cube3 follows that of the neighboring (in frequency) cube2. The following metrics were defined for each of cube0, cube1 and cube2:

- σ: the rms noise;
- $f_{\rm ex}$: fraction of the total number of pixels with an absolute value $>6.75\sigma$;
- $p_{0.8}$: ratio between the width of the noise histogram at a level of 0.8% of the maximum and σ.

The last two metrics were empirically determined to be successful at identifying deviations from Gaussianity in the noise histograms, which correspond to artifacts in the cubes (see Fig. 6).

Since the line cube quality can differ significantly from the continuum quality, upon which release of processed data is based (see Sects. 3.3.2 and 4.1), this first data release can contain cubes of poorer quality. Given this, rather than a strict pass/fail validation, a slightly more nuanced system of "good", "okay" and "bad" was adopted for line cube quality:

- Good: no (or very minor) artifacts;
- Okay: minor artifacts present but would not significantly impact analysis;
- Bad: major artifacts that have to be accounted for in analysis.

"Good" cubes satisfy all three of the following criteria:

1. $\sigma < 3$ mJy,
2. $\log(f_{\rm ex}) < -5.30$,
3. $p_{0.8} < 0.25 f_{\rm ex} + 5.875$.

"Okay" cubes fail to fulfill all of the "good" criteria but do meet all of the following conditions:

1. $\sigma < 3$ mJy,
2. $-5.30\log(f_{\rm ex}) < -4.52$,
3. $p_{0.8} < 0.5 f_{\rm ex} + 7.2$.

"Bad" cubes are those that do not meet the "good" or "okay" criteria. Using these conditions, we assigned all of cube0, cube1 and cube2 a ranking of "good", "okay" or "bad". Cube3 was assigned the quality of cube2 in all cases.

In order to determine the above criteria, a large number of cubes (∼550 cubes from 14 observations) were visually inspected. Figure 6 demonstrates the inspection plots, including the noise histogram, an image of a representative channel, and a position-velocity slice. Generally, the first criterion ensures a minimum sensitivity while the second two criteria identify deviations from Gaussianity in the noise distributions of the cubes.

6.2. Overview of released line cube quality

The validation of the line cubes can diverge quite significantly from that of the continuum images. This is because the two main causes of line cubes failing validation, incomplete continuum subtraction and bad frequency ranges (whether from heavy flagging due to RFI or subbands with poorly measured beamweights), can be independent of the quality of the

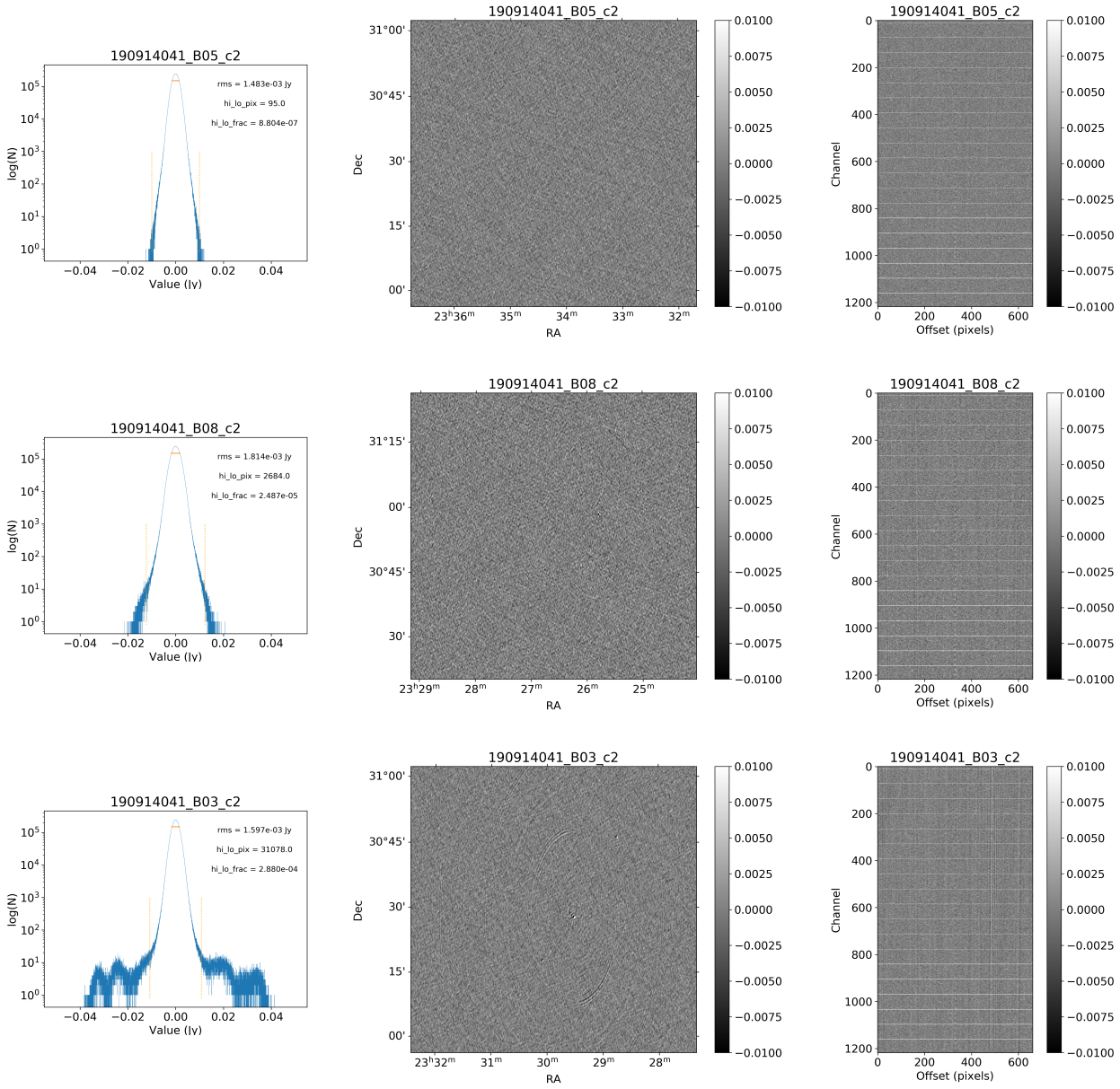

Fig. 6. Examples of the three quality classes used for the HI quality assessment. The top row shows an example of a "good" observation (ObsID 190914041, beam 5, cube 2), the middle one an "okay" observation (ObsID 190914041, beam 8, cube 2) and the bottom one a "bad" observation (ObsID 190914041, beam 3, cube 2). The columns show, from left to right, the noise histogram, an extract of the central velocity channel, and a position-velocity diagram through the center of the cube (the horizontal lines in the position-velocity diagrams are the subband edges; see Sect. 7.2). In the left column, the short horizontal line indicates the rms, σ, and the two dotted vertical lines indicate $\pm 6.75\sigma$. The "good" observation in the top row shows hardly any artifacts and a Gaussian noise histogram. The "okay" observation in the middle row shows a minor continuum subtraction artifact, which causes somewhat extended wings to the noise histogram. The "bad" observation in the bottom row shows significant continuum subtraction artifacts, resulting in a very non-Gaussian noise histogram.

continuum images and self-calibration[19]. As incomplete continuum subtraction can be addressed with a secondary subtraction in the image plane using the line cubes and bad frequency ranges are an unfortunate feature of radio observations, we do not require the line cubes to separately pass validation. Instead, the quality of the data cube ("G"ood, "O"kay, or "B"ad) is clearly indicated in the associated VO table (see Table 2). In total, 10 317 of the released cubes are good, while 1116 are okay, and 2063 are bad. Thus, over 75% of cubes fully pass validation while only 15% are rated as bad. The cubes with a quality assignment of bad may benefit from further off-line processing (i.e., continuum subtraction) before analysis.

Table 4 provides a look at the median rms values for the different spectral cubes across all the released cubes; the uncertainties represent the 16th and 84th percentiles. There is a trend that the noise values are slightly higher for the lower frequency cubes, consistent with a worsening RFI environment at lower frequencies, in addition to the fact that the system performance is generally worse at lower frequencies. Limiting the assessment to

[19] While poor continuum calibration is likely to lead to worse continuum subtraction, good continuum calibration does not ensure good continuum subtraction. In particular, poor bandpass calibration can lead to poor continuum subtraction.

only "good" cubes decreases the median noise values slightly, as would be expected, but the change is minor, thus supporting the strategy of releasing all cubes where the continuum image passes validation.

The median noise of 1.6 mJy beam^{-1} corresponds to a 3-σ column density sensitivity of 1.8×10^{20} atoms cm^{-2} over 20 km s^{-1}; this is for a median declination of 38° for released beams, which corresponds to an angular resolution of $24'' \times 15''$ for the spectral line cubes.

7. Known caveats

As described above, we have undertaken validation of produced data products in order to identify high quality data for release. However, there are a few global issues that affect data quality which we briefly describe below.

7.1. Ghosts

The Apertif data suffer from "ghosts" at the center of images: bad signal with random phase (that averages to zero). These ghosts are most prominent in channels 16 and 48 of each subband. While early versions of the Apercal pipeline flagged these channels, this was disabled for all data products presented here. Before the SVC period, the finite impulse response (FIR) filter in the channel filterbank was enabled. This severely reduced the presence of ghosts in channels 16 and 48, but did not completely remove them, and the ghost signal was also present at a low level across all channels. Due to the reduced presence of the ghosts in channels 16 and 48, plus the low level contribution from all channels, the decision was made to not flag channels 16 and 48 of the subbands as the extra bandwidth outweighed the presence of the ghosts. The presence of these ghosts builds up when averaging data over frequency, and so they affect all Apertif data products. Thus, any source identified at the exact center of a beam should be treated with extreme caution.

7.2. Aliasing

The coarse channelization of the data into subbands uses a filter that does not have a perfectly sharp frequency response. This results in some overlap of response between adjacent subbands. This effect is strongest for channels near a subband edge and also results in a sharp drop in overall response for channels at the subband edges, namely channels 0, 1 and 63 of every subband. No correction is done for the aliasing, and the pipeline uses a brute force approach of flagging the channels with suppressed signal at the subband edges. Thus, we note that 3 out of every 64 channels are flagged. Since cubes0-2 have a three channel averaging (which does not divide evenly into 64), the presence of these flagged channels shifts around, and the manifestation of this flagging alternates between a single channel that is fully flagged, or two adjacent channels that are partially flagged (1 or 2 of the 3 averaged channels)[20]. In addition, aliased signal may occur in the presence of extremely strong H I emission, but this will not impact the vast majority of H I detections.

8. Scientific potential

In this section, we briefly highlight the scientific potential of the data contained in this first data release.

[20] This accounts for the horizontal stripes in the right panels of Fig. 6.

8.1. Continuum images

The Apertif continuum images have three times the angular resolution of NVSS and are ∼10 times as sensitive. Thus, the Apertif images will both resolve more source structure and also detect fainter emission than NVSS. The upper two panels of Fig. 7 illustrate this, showing a mosaicked Apertif image (K22) and a NVSS image over the same field of view. Many more point sources are seen in the Apertif data, and the excellent surface brightness sensitivity of WSRT-Apertif combined with angular resolution, reveal the features of an extended, diffuse source. The sensitivity and resolution of the Apertif continuum images are comparable to those achieved by the Evolutionary Map of the Universe (EMU) survey with ASKAP (e.g., Gürkan et al. 2022); with complementary sky coverage the two surveys augment each other well.

Furthermore, as described in van Cappellen et al. (2022, see also their Fig. 3), the depth and angular resolution of the Apertif continuum images nicely match with the images produced by the LOFAR surveys. The synergy is particularly strong with LoTSS at 150 MHz and LoLSS at 42–66 MHz, both aiming at covering the entire northern sky. The left side of Fig. 7 demonstrates the comparison between Apertif and LoTSS data. The combination Apertif-LOFAR is particularly relevant for the study of the spectral properties of radio sources. The sensitivity of the surveys with the two instruments is well suited to trace the typical spectral index observed in extragalactic sources, around $\alpha \sim 0.7$ or steeper[21]. Specifically, given the relatively high spatial resolution, it is possible to derive resolved spectral index images (as illustrated in the bottom right panel of Fig. 7) for both single objects and large samples. In particular, significant steepening of the spectrum at low frequencies reveals the presence of a particularly old electron population, possibly indicating remnant emission where the nuclear activity has stopped and the electrons have not been replenished. Morganti et al. (2021a,b) presented searches for structures with such extremely steep spectral indices by combining Apertif and LOFAR 150 MHz images in the Lockman Hole region. Finding samples of these elusive objects allows us to put constraints on their life-cycle (see Jurlin et al. 2020; Morganti et al. 2021b). Resolved spectral index studies are also important for diffuse emission in clusters (Orrù et al., in prep.; Shulevski et al., in prep.), for single objects like the radio galaxy B2 1321+31 (Morganti et al. 2021a) as well as for large major mergers like Mrk 273 (Kukreti et al. 2022). These studies will be further expanded by the combination with the LBA LOFAR survey, as seen in the study of Mrk 273 (Kukreti et al. 2022).

The east-west nature of WSRT means that if a source varies during the course of an observation, it leaves a very clear pattern in the images. Oosterloo et al. (2020) used this to identify an intra-hour variable during the SVC, which was then monitored as a medium-deep field over the course of full operations. To date, about twenty intra-hour variables have been identified in the Apertif survey data, along with a few radio variable stars (Oosterloo et al., in prep.).

The image products in this data release will also complement any future independent detections of transients and variables in the area it covers. This has recently been demonstrated for both fast radio bursts and for radio afterglows of gravitational-wave events. Connor et al. (2020) detected a bright fast radio burst in the Apertif time-domain survey (Oostrum et al. 2020), and then used the Apertif continuum image to set limits on any

[21] In this paper, the spectral index α is defined through $S \propto \nu^{-\alpha}$, where S is flux density and ν the frequency.

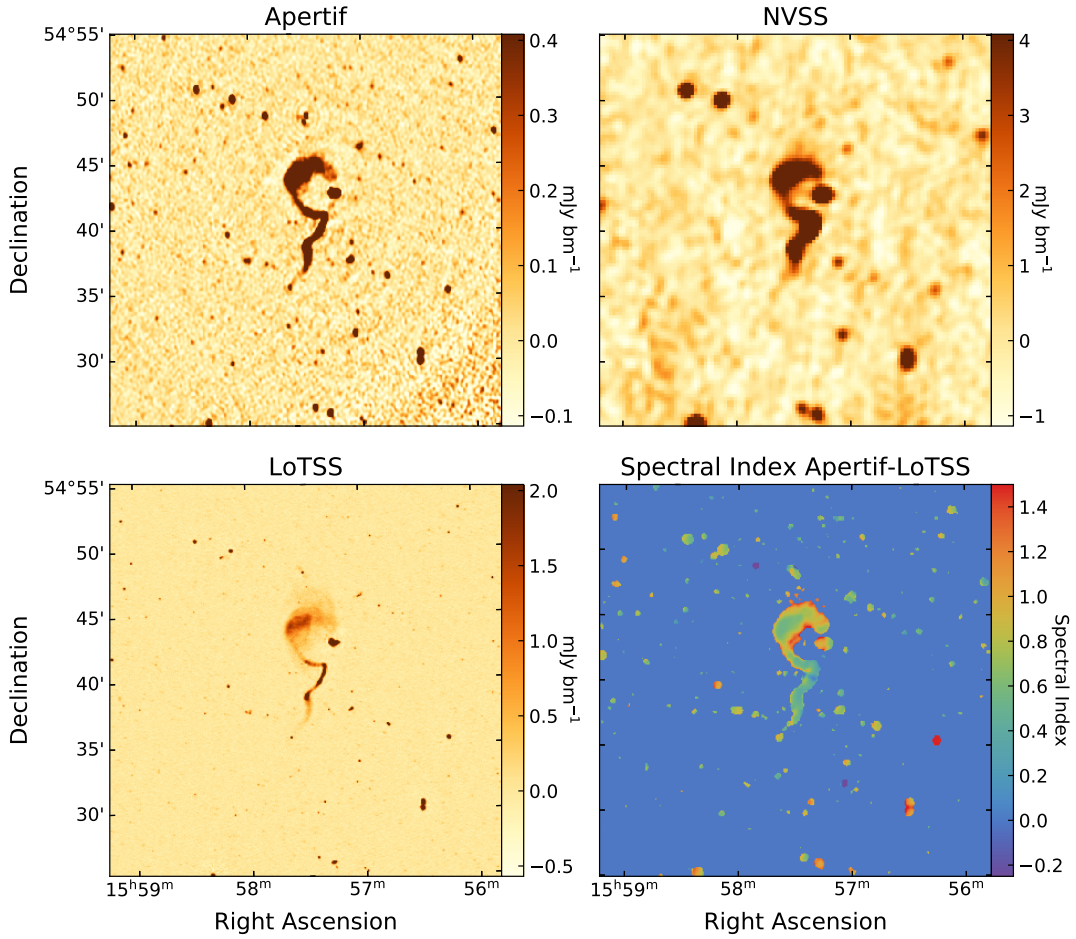

Fig. 7. Example Apertif continuum image with comparison to NVSS and LoTSS. *Upper left:* Apertif continuum image, mosaicked as described in K22. *Upper right:* NVSS image of the same field (Condon et al. 1998). *Lower left:* LoTSS image of the same field (Shimwell et al. 2022), with the scaling set so that a point source with a spectral index of 0.7 has the same brightness as in the Apertif image. *Lower right:* spectral index image between the Apertif and LoTSS image.

accompanying persistent radio source. Boersma et al. (2021) searched Apertif data for a radio counterpart to binary neutron-star merger gravitational-wave event GW190425. While none was found for that particular event, future searches can use DR1 as the baseline comparison for the radio-afterglow detection.

The companion paper K22 provides a continuum source catalog based on all continuum images contained in this data release. This includes a comparison to NVSS to identify sources that vary on long time scales, plus a cross-match to the LoTSS DR1 to provide spectral indices for unresolved sources.

8.2. Polarization images and cubes

The Apertif polarization data, as with the continuum data, provide an improvement of three times the angular resolution and more than ten times the sensitivity when compared to NVSS, the current benchmark for wide surveys of the polarized sky. The sensitivity of the wide tier results in a polarized source density of 21 sources deg^{-2} (Adebahr et al. 2022a), a factor of 20 improvement compared to NVSS (Taylor et al. 2009). This increased density of polarized sources enables a higher angular resolution rotation measure map to be constructed, thus providing a more detailed look at the magnetic field of our own Milky Way galaxy. The sensitivity of the Apertif surveys also means that the polarized sky is being measured down to the μJy level. An open question is at what level the polarized sky changes from being dominated by AGN to star-forming galaxies; this happens at a lower flux level than for the total power radio continuum sky. Adebahr et al. (2022a) use early Apertif data to show that polarized source counts are still dominated by AGN, but that the AGN are hosted in late-type, rather than early-type, galaxies. Additionally, the high density of polarized sources in the Apertif data provides the possibility to robustly investigate the source counts of polarized sources and behavior of fractional polarization with total intensity (Berger et al., in prep.).

The synergy with LOFAR, and LoTSS in particular, is also key for polarization. Having information over a decade in frequency allows not only an investigation of the polarization behaviour with respect to the sources' spectral index, but also an investigation of polarization spectra. Due to Faraday Dispersion being strongly wavelength dependent, depolarisation effects are much more dominant at longer wavelengths. Combining LOFAR and Apertif data thus allows a deep insight into the nature of depolarisation mechanisms and their physical origins (Berger et al., in prep.). Such an analysis also provides information on the morphology and turbulence of the magnetic fields, not only in the host objects, where the polarised emission is generated, but also along the line-of-sight to the observer. When using additional redshift information this enables an analysis of the evolution of cosmic magnetic fields (Berger et al. 2021).

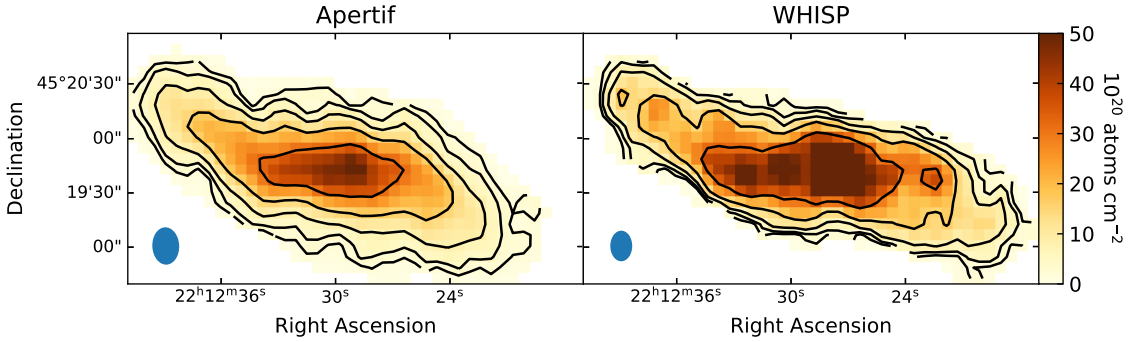

Fig. 8. H I content of UGC 11951 as detected in both Apertif (*left*) and WHISP (*right*). The color scale is the same between the two images and the contours are at [2, 4, 8, 16, 32] $\times 10^{20}$ atoms cm^{-2}. We note that the WHISP data have a smaller beam size as uniform weighting was used; this can also account for the difference in peak column density values between the two images. The Apertif data is from a single beam; mosaicking would further increase the signal in that map.

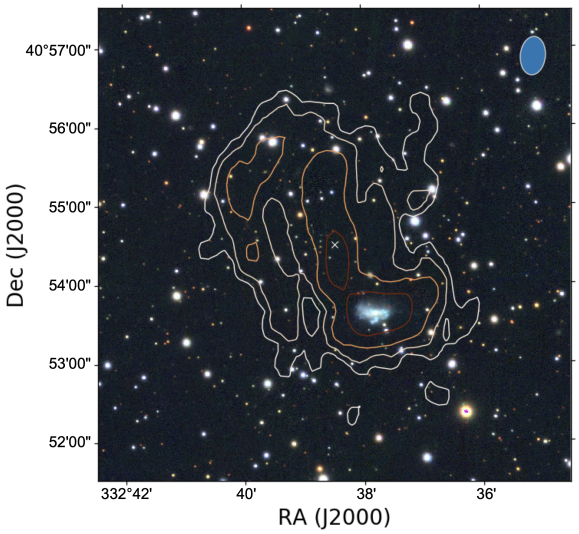

Fig. 9. Example of a H I-detected galaxy within the released spectral line cubes. The angular resolution provided by the Apertif surveys reveal that the H I disk is hugely extended beyond the stellar disk. The H I contours are at [2, 4, 8, 16] $\times 10^{20}$ atoms cm^{-2}.

8.3. Spectral line cubes

The Apertif spectral line cubes offer angular resolution combined with an untargeted detection of line emission, independent of the stellar content of galaxies. Compared to single-dish H I surveys, such as the ALFALFA H I survey, the angular resolution improves by >10×, allowing the distribution of the H I to be studied, providing information on disturbed morphology and environmental effects, resolved kinematics, and more. In terms of sensitivity and angular resolution, the wide tier is well-matched to WHISP, a targeted survey of 375 galaxies with WSRT (van der Hulst et al. 2001). Figure 8 shows UGC 11951 as seen in both Apertif and WHISP, where both datasets show a warp in the H I disk. The Apertif spectral cubes offer WHISP-quality data but for thousands of galaxies, with no selection criteria based on the stellar content. This enables the detection of galaxies with minimal stellar content, and the derivation of their kinematic properties to study their behavior on galaxy scaling relations (Šiljeg et al., in prep.). The Apertif H I detections are being used to select galaxies, based on their H I morphology, for observation with the large IFU of the new WEAVE instrument (Jin et al., in prep.), as part of the WEAVE-Apertif survey. Figure 9 demonstrates the power of the angular resolution combined with untargeted selection, showing a galaxy with a hugely extended H I disk whose stellar content appears relatively undisturbed.

The Apertif spectral line cubes are not solely H I cubes but OH megamasers can also be detected over their frequency coverage. Hess et al. (2021) report the serendipitous discovery of an OH megamaser in the Apertif spectral line cubes and discuss expectations for the full Apertif imaging surveys, including how the wide bandwidth permits the simultaneous detection or placement of limits on OH megamaser satellite lines in addition to detecting the redshifted main lines.

9. Future prospects

This is the first of multiple data releases to come from the Apertif imaging surveys. Improvements offered by future data releases can be broken into three broad categories:

More sky coverage. As the processing of the Apertif imaging survey data continues, there will be more processed data that can naturally be released in the same manner as this data release.

Improved data processing. A major component of this release was to determine which data products were of high enough quality to be released. Improvements to the data processing will result in more high quality data to release, improving the overall sky coverage of the public data.

Higher order data products. This release initially provides per-beam images and cubes. A companion paper K22 provides a continuum source catalog. The ultimate goal is to offer more advanced science products to the community. This includes mosaicked images, but also source cutouts and cubelets and source catalogs for all data products (polarization and spectral line). For example, Adebahr et al. (2022a) provide a polarized source catalog for the SVC observations.

Below, we detail a few of the key processing improvements that are in progress, which we plan to incorporate in future data releases.

Direction dependent calibration. In some images produced with `Apercal`, there are direction dependent errors (DDEs) remaining around sources. We believe these errors come from two main sources: (1) pointing errors in the dishes and (2) faulty PAF elements leading to specific compound beams on a given dish having a non-ideal beam response that is different from

other dishes (see Dénes et al. (2022) for more details). These errors cannot be removed in the standard self-calibration procedure implemented in `Apercal`. We took operational steps to address these errors, updating the pointing model and targeted maintenance of faulty elements. However, there will always be some bad elements, and hence compound beams with bad shapes. Thus, we are also working on including direction-dependent calibration in `Apercal`, where the antenna gains are solved in the directions of bright sources simultaneously, pushing the amplitude of artifacts below the thermal noise level.

Two-stage continuum subtraction. The single-stage continuum subtraction is not sufficient in many (∼20%) cases. Implementing a second continuum subtraction step will increase the quality of the final line cubes by minimizing the presence of continuum artifacts.

Subband-edge flagging. The lack of an anti-aliasing filter results in suppressed signal on subband edges; the current approach to handling this is to flag three of every sixty-four channels, significantly affecting the final line cubes. This is likely an overly generous flagging approach and only the first channel of every sixty-four needs to be flagged, while the bandpass correction can account for the subband response in the second and last channels of each subband.

Mosaicking. We are also working on a mosaicking procedure so that in future data releases, mosaics (both of single Apertif pointings and also across pointings) can be released in addition to individual beam images. K22 provides an overview of a mosaicking tool used in the creation of the continuum catalog that undertakes the different primary beam correction for various Apertif beams, including a link to source code.

10. Summary

This paper presents the first release of data products from the Apertif imaging surveys, covering the first year of survey observations. The release consists of two major components: the raw observational data, plus processed data products. The raw observational data covers 300 MHz of bandwidth with 12.2 kHz resolution and provide an angular resolution up to $11''/\sin\delta$. This data release consists of 221 observations of 160 unique survey fields, corresponding to an effective sky coverage of $\sim$1000 deg^2.

Processed data products available include continuum images, Stokes V images, Stokes Q and U cubes, and four spectral line cubes plus associated dirty beams. The processed data products have a bandwidth of 137.5 MHz; the lower 162.5 MHz of the band is discarded due to strong RFI. We release all processed data products for beams where the continuum image passes validation, consisting of 3374 observations of 2683 unique field-beam combinations. A total of 44% of all possible beams are released. The main reasons for continuum images to fail validation are artifacts from poor self-calibration or direction-dependent errors, both of which will be addressed in future versions of the pipeline.

The metrics and validation status of all data products are provided in the associated VO tables (Table 2). The continuum images have a median inner noise of 41.4 μJy beam^{-1}; the Stokes V images have a median inner noise of 36.9 μJy beam^{-1}; and the spectral line cubes have a median noise of 1.6 mJy beam^{-1} over 36.6 kHz. The median angular resolution of the continuum images and polarization data is $11.6''/\sin(\delta)$.

Acknowledgements. We wish to thank the anonymous referee for useful comments that improved the quality and structure of this paper. This work makes use of data from the Apertif system installed at the Westerbork Synthesis Radio Telescope owned by ASTRON. ASTRON, the Netherlands Institute for Radio Astronomy, is an institute of the Dutch Research Council ("De Nederlandse Organisatie voor Wetenschappelijk Onderzoek, NWO). Apertif was partly financed by the NWO Groot projects Apertif (175.010.2005.015) and Apropos (175.010.2009.012). This work was partly supported by funding from the European Research Council under the European Union's Seventh Framework Programme (FP/2007-2013), through ERC Grant Agreement No. 291531 ('HIStoryNU', PI: JMvdH) and ERC Advanced Grant RADIOLIFE-320745 (PI: RM), in addition to funding from NWO via grant TOP1EW.14.105 (PI: TAO). E.A.K.A. is supported by the WISE research programme, which is financed by NWO. B.A. acknowledges funding from the German Science Foundation DFG, within the Collaborative Research Center SFB1491 "Cosmic Interacting Matters - From Source to Signal". KMH acknowledges financial support from the State Agency for Research of the Spanish Ministry of Science, Innovation and Universities through the "Center of Excellence Severo Ochoa" awarded to the Instituto de Astrofísica de Andalucía (SEV-2017-0709), from the coordination of the participation in SKA-SPAIN, funded by the Ministry of Science and Innovation (MCIN). OMB and JvL acknowledge funding from NWO under the Vici research program "ARGO" with project number 639.043.815. Y.M., L.C.O., R.S. and J.vL. acknowledge funding from the European Research Council under the European Union's Seventh Framework Programme (FP/2007–2013)/ERC Grant Agreement No. 617199 ("ALERT"). IPM acknowledges funding from the Netherlands Research School for Astronomy (grant no. NOVA5-NW3-10.3.5.14). A.A.P. acknowledges support of the STFC consolidated grant ST/S000488/1. DV acknowledges support from the Netherlands eScience Center (NLeSC) under grant ASDI.15.406. This research has made use of NASA's Astrophysics Data System Bibliographic Services and Astropy, (`http://www.astropy.org`) a community-developed core Python package for Astronomy (Astropy Collaboration 2013, 2018).

References

Adebahr, B., Berger, A., Adams, E. A. K., et al. 2022a, A&A, 663, A103
Adebahr, B., Schulz, R., Dijkema, T. J., et al. 2022b, Astron. Comput., 38, 100514
Allison, J. R., Sadler, E. M., Amaral, A. D., et al. 2022, PASA, 39, e010
Astropy Collaboration (Robitaille, T. P., et al.) 2013, A&A, 558, A33
Astropy Collaboration (Price-Whelan, A. M., et al.) 2018, AJ, 156, 123
Berger, A., Adebahr, B., Herrera Ruiz, N., et al. 2021, A&A, 653, A155
Condon, J. J., Cotton, W. D., Greisen, E. W., et al. 1998, AJ, 115, 1693
Boersma, O. M., van Leeuwen, J., Adams, E. A. K., et al. 2021, A&A, 650, A131
Connor, L., van Leeuwen, J., Oostrum, L. C., et al. 2020, MNRAS, 499, 4716
de Gasperin, F., Williams, W. L., Best, P., et al. 2021, A&A, 648, A104
Dénes, H., Hess, K. M., Adams, E. A. K., et al. 2022, A&A, in press, `https://doi.org/10.1051/0004-6361/202244045`
Gaensler, B. M., Landecker, T. L., Taylor, A. R., & POSSUM Collaboration 2010, in American Astronomical Society Meeting Abstracts, 215, 470.13
Gürkan, G., Prandoni, I., O'Brien, A., et al. 2022, MNRAS, 512, 6104
Hale, C. L., McConnell, D., Thomson, A. J. M., et al. 2021, PASA, 38, e058
Haynes, M. P., Giovanelli, R., Kent, B. R., et al. 2018, ApJ, 861, 49
Hess, K. M., Roberts, H., Dénes, H., et al. 2021, A&A, 647, A193
Jarvis, M., Taylor, R., Agudo, I., et al. 2016, in MeerKAT Science: On the Pathway to the SKA, 6
Jurlin, N., Morganti, R., Brienza, M., et al. 2020, A&A, 638, A34
Koribalski, B. S., Staveley-Smith, L., Westmeier, T., et al. 2020, Ap&SS, 365, 118
Kukreti, P., Morganti, R., Bondi, M., et al. 2022, A&A, 664, A25
Kutkin, A., Morganti, R., Oosterloo, T., et al. 2022, A&A, in press, `https://doi.org/10.1051/0004-6361/202244008`
Lacy, M., Baum, S. A., Chandler, C. J., et al. 2020, PASP, 132, 035001
Maan, Y., & van Leeuwen, J. 2017, in 2017 XXXIInd General Assembly and Scientific Symposium of the International Union of Radio Science (URSI GASS, 2)
Maddox, N., Jarvis, M. J., & Oosterloo, T. A. 2016, MNRAS, 460, 3419
Maddox, N., Frank, B. S., Ponomareva, A. A., et al. 2021, A&A, 646, A35
McConnell, D., Hale, C. L., Lenc, E., et al. 2020, PASA, 37, e048
McMullin, J. P., Waters, B., Schiebel, D., Young, W., & Golap, K. 2007, in Astronomical Data Analysis Software and Systems XVI, eds. R. A. Shaw, F. Hill, & D. J. Bell, Astronomical Society of the Pacific Conference Series, 376, 127
Meyer, M. J., Zwaan, M. A., Webster, R. L., et al. 2004, MNRAS, 350, 1195
Morganti, R., Jurlin, N., Oosterloo, T., et al. 2021a, Galaxies, 9, 88
Morganti, R., Oosterloo, T. A., Brienza, M., et al. 2021b, A&A, 648, A9
Norris, R. P., Marvil, J., Collier, J. D., et al. 2021, PASA, 38, e046
Offringa, A. R. 2016, A&A, 595, A99

Offringa, A. R., van de Gronde, J. J., & Roerdink, J. B. T. M. 2012, A&A, 539
Oosterloo, T. A., Vedantham, H. K., Kutkin, A. M., et al. 2020, A&A, 641, L4
Oostrum, L. C., Maan, Y., van Leeuwen, J., et al. 2020, A&A, 635, A61
Rengelink, R. B., Tang, Y., de Bruyn, A. G., et al. 1997, A&AS, 124, 259
Sault, R. J., Teuben, P. J., & Wright, M. C. H. 1995, in Astronomical Data Analysis Software and Systems IV, eds. R. A. Shaw, H. E. Payne, & J. J. E. Hayes, Astronomical Society of the Pacific Conference Series, 77, 433
Shimwell, T. W., Tasse, C., Hardcastle, M. J., et al. 2019, A&A, 622, A1
Shimwell, T. W., Hardcastle, M. J., Tasse, C., et al. 2022, A&A, 659, A1
Smith, M. W. L., Ibar, E., Maddox, S. J., et al. 2017, ApJS, 233, 26
Taylor, M. B. 2005, in Astronomical Data Analysis Software and Systems XIV, eds. P. Shopbell, M. Britton, & R. Ebert, Astronomical Society of the Pacific Conference Series, 347, 29
Taylor, A. R., Stil, J. M., & Sunstrum, C. 2009, ApJ, 702, 1230
van Cappellen, W. A., Oosterloo, T. A., Verheijen, M. A. W., et al. 2022, A&A, 658, A146
van der Hulst, J. M., van Albada, T. S., & Sancisi, R. 2001, in Gas and Galaxy Evolution, eds. J. E. Hibbard, M. Rupen, & J. H. van Gorkom, Astronomical Society of the Pacific Conference Series, 240, 451
van Leeuwen, J., Kooistra, E., Oostrum, L., et al. 2022, ArXiv e-prints [arXiv:2205.12362]
Wayth, R. B., Lenc, E., Bell, M. E., et al. 2015, PASA, 32, e025
White, R. L., Becker, R. H., Helfand, D. J., & Gregg, M. D. 1997, ApJ, 475, 479

[1] ASTRON, the Netherlands Institute for Radio Astronomy, Oude Hoogeveensedijk 4,7991 PD Dwingeloo, The Netherlands
e-mail: adams@astron.nl
[2] Kapteyn Astronomical Institute, PO Box 800, 9700 AV Groningen, The Netherlands
[3] Astronomisches Institut der Ruhr-Universität Bochum (AIRUB), Universitätsstrasse 150, 44780 Bochum, Germany
[4] Department of Astronomy, University of Cape Town, Private Bag X3, Rondebosch 7701, South Africa
[5] Instituto de Astrofísica de Andalucía (CSIC), Glorieta de la Astronomía s/n, 18008 Granada, Spain
[6] Astro Space Center of Lebedev Physical Institute, Profsoyuznaya Str. 84/32, 117997 Moscow, Russia
[7] Department of Physics, Virginia Polytechnic Institute and State University, 50 West Campus Drive, Blacksburg, VA 24061, USA
[8] CSIRO Astronomy and Space Science, Australia Telescope National Facility, PO Box 76, Epping, NSW 1710, Australia
[9] Sydney Institute for Astronomy, School of Physics, University of Sydney, Sydney, New South Wales 2006, Australia
[10] Anton Pannekoek Institute, University of Amsterdam, Postbus 94249, 1090 GE Amsterdam, The Netherlands
[11] NIKHEF, National Institute for Subatomic Physics, Science Park 105, 1098 XG Amsterdam, The Netherlands
[12] Cahill Center for Astronomy, California Institute of Technology, Pasadena, CA, USA
[13] Department of Electrical Engineering, Chalmers University of Technology, Gothenburg, Sweden
[14] Max-Planck-Institut für Radioastronomie, Auf dem Hügel 69, 53121 Bonn, Germany
[15] Department of Physics and Electronics, Rhodes University, PO Box 94, Makhanda 6140, South Africa
[16] National Centre for Radio Astrophysics, Tata Institute of Fundamental Research, Pune 411007, Maharashtra, India
[17] Netherlands eScience Center, Science Park 402, 1098 XH Amsterdam, The Netherlands
[18] Department of Physics and Astronomy, West Virginia University, White Hall, PO Box 6315, Morgantown, WV 26506, USA
[19] Center for Gravitational Waves and Cosmology, West Virginia University, Chestnut Ridge Research Building, Morgantown, WV 26505, USA
[20] Oxford Astrophysics, Denys Wilkinson Building, University of Oxford, Keble Rd, Oxford OX1 3RH, UK
[21] Tricas Industrial Design & Engineering, Zwolle, The Netherlands
[22] University of Oslo Center for Information Technology, PO Box 1059, 0316 Oslo, Norway

Appendix A: Additional available data

In addition to the release of survey data, imaging data from before the start of survey operations are also available. These data are not hosted via VO tables but can be accessed via requests to the ASTRON helpdesk[22].

Appendix A.1. Data from the science verification campaign

Before the start of survey operations, the SVC was undertaken to verify the scientific performance of the Apertif system. The goal of this period was to take data in as close to final survey mode as possible to verify the science performance of Apertif before the start of surveys. The good quality data from this period, including processed imaging data products, were publicly released at the end of 2019. In this Appendix we briefly describe the imaging observations and data quality that are part of this earlier release.

Appendix A.1.1. Observations and processing

The target fields and associated calibrators for the SVC period are listed in Table A.2. During the SVC period, the observing frequency range was 1250-1550 MHz. The data was processed with a 150 MHz version of the pipeline specific to the SVC period[23]. The frequency range of the final data products is close, but not quite identical to that used for the survey data products (1291.8–1441.8 MHz for the SVC data). However, the line cubes are produced over the same frequency range (given in Table 3). One key processing difference compared to the survey processing is that the SVC data required an extra offline correction for the delay tracking; this correction is done online on the datawriter during survey observations (see Sect. 8.3 of van Cappellen et al. (2022)).

Appendix A.1.2. SVC data quality

The processed SVC data was released without validation as a demonstrator of data quality, both the intrinsic quality and pipeline processing. For comparison to the survey data release, Table A.1 provides a high-level overview of the number of beams that would have passed continuum validation for each field, if the validation process as for the survey data release had been used.

Appendix A.2. Early science observations

There was a ~2.5 month period between the SVC and start of survey operations. This period was focused on development and finalizing tools for operations but did offer the possibility for high quality early science observations. These observations are listed in Table A.3. These data were observed at different frequency settings and only the last observations have the online correction for delay tracking. We are releasing these observations but not associated processed data; none of these observations have been fully processed by the Apercal pipeline. We do note that one field (ObsID 190428055) was calibrated with Apercal and manually imaged and published in Morganti et al. (2021b).

Table A.1. Summary of continuum validation for SVC beams

Field	Pass	Fail
S2248+33[a]	26	3
M1403+53[b]	4	34
M0155+33[b]	6	32
S2246+38[b]	15	23
S1415+36[b]	24	14

Notes. [a] Twenty-nine beams processed [b] Thirty-eight beams processed.

[22] https://support.astron.nl/jira/servicedesk
[23] The SVC specific version of the pipeline is available at https://github.com/apertif/apercal/releases/tag/v2.4

Table A.2. Overview of the imaging SVC fields

Field		Flux calibrator			Polarization calibrator		
Name	Task ID	Name	Task IDs	t_{obs} min	Name	Task IDs	t_{obs} min
S2248+33[a]	190409015	3C196	190408125-150 190409001-014[a]	5	3C138	190409016-055	4
M1403+53	190409056	3C196	190410002-041	5	3C138	190409016-055	4
M0155+33	190410001	3C196	190410002-041	5	3C138	190409016-055	4
S2246+38	190411001	3C196	190410002-041	5	3C138	190411002-041	4
S1415+36	190411042	3C196[b]	190410002-041[b]	5	3C138	190411002-041	4

Notes. [a] Beams 31-39 failed (190409006-14 not on source) [b] Non-bracketing flux calibrator used due to failure of observing session

Table A.3. Overview of the imaging early science fields

Field		Flux calibrator		Polarization calibrator				
Name	ObsID	Name	ObsIDs	Name	ObsIDs	Freq MHz	DT[a]	Notes
1530+29	190419137	3C147	190419097−136	3C138	190420001−40	1250−1550	N	RTC&RTD bad
1530+29	190424047	3C147	190424007−46	–	–	1250−1550	N	RTC&RTD bad
LH_WSRT	190428055	3C147	190428016−54	3C286	190429001−40	1250−1550	N	
LH_WSRT	190505048	3C147	190505008−47	3C286	190506001−40	1220−1520	N	
M31	190511013	3C147	190512001−40	3C286	190510107−190511012	1220−1520	N	
M1403+53	190511014	3C147	190512001−40	3C286	190510107−190511012	1220−1520	N	
LH_GRG	190601059	3C147	190601019−58	–	–	1220−1520	N	
LH_GRG	190602049	3C147	190602009−48	3C286	190602050−190603031	1130−1430	N	
M1403+53	190608061	3C147	190609001−40	3C138	190608021−60	1220−1520	N	no RTD; delay center offset = [0.33,0]
M81	190609041	3C48	190610001−40	3C138	190610041−80	1220−1520	N	no RTD
M81_offset2	190610081	3C48	190610001−40	3C138	190610041−80	1220−1520	N	no RTD
S2258+29	190629059	3C147	190629018−57	3C138	190630001-40	1130 − 1430	Y	
S1349+26	190630041	3C147	190701001−41	3C138	190630001−40	1130−1430	Y	
M0142+31	190701001	3C147	190701002−41	3C138	190630001-40	1130−1430	Y	

Notes. [a]Whether online delay tracking (DT) was active or not.